

# Full-counting statistics for molecular junctions, the fluctuation theorem and singularities

Y. Utsumi,<sup>1,\*</sup> O. Entin-Wohlman,<sup>2,†</sup> A. Ueda,<sup>3</sup> and A. Aharony<sup>2,†</sup>

<sup>1</sup>*Department of Physics Engineering, Faculty of Engineering, Mie University, Tsu, Mie, 514-8507, Japan*

<sup>2</sup>*Department of Physics and the Ilse Katz Center for Meso- and Nano-Scale Science and Technology,  
Ben Gurion University, Beer Sheva 84105, Israel*

<sup>3</sup>*Faculty of Pure and Applied Sciences, Division of Applied Physics,  
University of Tsukuba, Tsukuba, Ibaraki, 305-8573, Japan*

(Dated: October 9, 2012)

We study the full-counting statistics of charges transmitted through a single-level quantum dot weakly coupled to a local Einstein phonon which causes fluctuations in the dot energy. An analytic expression for the cumulant-generating function, accurate up to second order in the electron-phonon coupling and valid for finite voltages and temperatures, is obtained in the extended wide-band limit. The result accounts for nonequilibrium phonon distributions induced by the source-drain bias voltage, and concomitantly satisfies the fluctuation theorem. Extending the counting field to the complex plane, we investigate the locations of possible singularities of the cumulant-generating function, and exploit them to identify regimes in which the electron transfer is affected differently by the coupling to the phonons. Within a large-deviation analysis, we find a kink in the probability distribution, analogous to a first-order phase transition in thermodynamics, which would be a unique hallmark of the electron-phonon correlations.

PACS numbers: 05.30.-d, 72.70.+m, 71.38.-k, 73.63.Kv, 05.70.Ln

## I. INTRODUCTION

It has been revealed in electric transport measurements that the electron-phonon interaction induces unique features in the nonequilibrium current through molecular junctions<sup>1,2</sup> and atomic wires.<sup>3-5</sup> In particular, when the phonon energy is small compared to the resonance width on the junction, the inelastic phonon scattering increases/decreases the current for small/large transmission probabilities as the source-drain bias voltage  $V$  exceeds the local phonon frequency  $\omega_0$ .<sup>1,3-5</sup> Quite a number of theoretical microscopic models, e.g. Ref. 6, including density-functional theories,<sup>7</sup> have been devoted to such junctions (see Ref. 8 and references therein). They revealed that a simplified model,<sup>9</sup> of a single-level quantum dot coupled to a local Einstein phonon mode causing fluctuations of the dot energy level,<sup>10</sup> seems to suffice to capture this ubiquitous feature. Recently, the current noise of an atomic wire has been measured,<sup>5</sup> and it was observed that the electron-phonon interaction can enhance or reduce the noise, depending on the value of the transmission probability. Based on the theory of Avriller and Levy Yeyati,<sup>11</sup> the negative correction is understood as resulting from the anti-bunching of two electrons: An electron cannot be inelastically scattered by a phonon when the final state is already occupied by another electron.

Avriller and Levy Yeyati considerations follow from the theory of full-counting statistics (FCS),<sup>12,13</sup> which is most convenient for analyzing nonequilibrium electric transport. Indeed, considerable effort has been invested in recent years in exploiting FCS to study various aspects of nonequilibrium quantum transport [e.g. Refs. 11–24 and references therein]. FCS refers to the probability

distribution  $P_\tau(q)$  of the charge  $q$  transmitted through a quantum conductor during a certain measurement time  $\tau$  at out-of-equilibrium conditions (we set  $e = \hbar = 1$ ). The effect of coupling to a vibrational mode on the electric transport has also been investigated in this context, both for a weak<sup>11,19-21</sup> and a strong<sup>22-24</sup> electron-phonon coupling.

In general, it is a rather formidable task to calculate the FCS of interacting electrons. For this reason, most of the investigators have taken advantage of the Keldysh field-theory technique. There, the characteristic function (CF),

$$\mathcal{Z}_\tau(\lambda) = \sum_q P_\tau(q) e^{iq\lambda}, \quad (1)$$

or the scaled cumulant-generating function (CGF)<sup>25</sup> pertaining to the steady state,

$$\mathcal{F}(\lambda) = \lim_{\tau \rightarrow \infty} \frac{1}{\tau} \ln \mathcal{Z}_\tau(\lambda), \quad (2)$$

can be formally written as a ‘partition function’ or a ‘free energy’, respectively, defined along the Keldysh time-contour. The  $\lambda$  appearing in these formulae is termed the counting field or the counting parameter. However, even if one calculates the CGF successfully, one still needs to find a way to characterize the electronic correlations in it. One promising approach would be to utilize the location distribution of the zeros of the CF, or equivalently that of the singularities of the CGF, by allowing the counting field  $\lambda$  in Eq. (1) to attain complex values,<sup>26-29</sup> similarly to the Yang-Lee theory of phase transition.<sup>30</sup> This idea is based on the recent observation that, upon transforming  $\lambda$  into  $u$ ,

$$u = e^{i\lambda}, \quad (3)$$

the singularities of the CGF of noninteracting electrons transported between two terminals are all on the negative real axis of the  $u$ -plane.<sup>26,31,32</sup> It suggests that singularities off the negative real axis would characterize electronic correlations. From this aspect, molecular junctions are rather advantageous since second-order perturbation theory in the electron-phonon coupling would capture most relevant features of the electron-phonon correlations in them, allowing for obtaining the location distribution of the singularities.

Another recent ingredient is the fluctuation theorem (FT).<sup>33–44</sup> The FT is a consequence of micro-reversibility and can be understood as a microscopic extension of the second law of thermodynamics. Despite its simple appearance, a detailed-balance like relation [see Eq. (6) below], the FT reproduces the linear-response results, i.e. it ensures the fluctuation-dissipation theorem and Onsager's reciprocal relations close to equilibrium,<sup>34–39</sup> while conveying invaluable information at nonequilibrium conditions. For molecular junctions, the FT has been addressed using the master-equation approach of FCS for incoherent electron transport.<sup>22,23</sup> The FT is considered to be a basic symmetry, such as gauge invariance, which the CF should fulfill.

In the present paper we investigate the FCS of electrons coupled to phonons under out-of-equilibrium conditions. Our calculation is accurate up to second order in the electron-phonon coupling. We begin in Sec. II with brief general explanations of the FT, the large-deviation analysis and singularities of the CGF. We then introduce in Sec. III the model Hamiltonian and present analytical results for the CGF and detailed explanations of the calculations and the approximations involved. A general formulation based on the nonequilibrium Luttinger-Ward potential<sup>45–47</sup> is relegated to Appendix A. In Sec. IV we analyze the singularities of the CGF and demonstrate the probability distribution within the large-deviation analysis. Section V summarizes our results.

## II. THE FLUCTUATION THEOREM AND SINGULARITIES

The definition of the probability distribution  $P_\tau(q)$  in quantum systems requires special care.<sup>12,13</sup> Full-counting statistics theory begins with introducing the CF [see Eq. (1) and Eq. (14) below for the definition employed in the Keldysh technique] and then defining the quasi-probability distribution by the inverse Fourier transform of the CF,

$$P_\tau(q) = \frac{1}{2\pi} \int_{-\pi}^{\pi} d\lambda e^{-i\lambda q} \mathcal{Z}_\tau(\lambda). \quad (4)$$

More details are given in Sec. III. The  $n$ -th cumulant, in steady state, is given by the  $n$ -th derivative of the CGF,

Eq. (2),

$$\langle\langle I^n \rangle\rangle = \lim_{\tau \rightarrow \infty} \frac{\langle\langle q^n \rangle\rangle}{\tau} = \left. \frac{\partial^n \mathcal{F}(\lambda)}{\partial (i\lambda)^n} \right|_{\lambda=0}. \quad (5)$$

For example, the average current is the first cumulant, and the current noise is the second one.

The FT in the context of quantum electric transport relates the probability of the current to flow oppositely to the bias voltage because of thermal agitations,  $P_\tau(-q)$ ,<sup>34–40</sup> to the distribution  $P_\tau(q)$ ,

$$P_\tau(-q) = P_\tau(q) e^{-\beta q V}, \quad (6)$$

where  $\beta$  is the inverse temperature. The FT can be equivalently written in terms of the CGF  $\mathcal{F}$ , Eq. (2), as

$$\mathcal{F}(\lambda) = \mathcal{F}(-\lambda + i\beta V). \quad (7)$$

The relation (7) restricts the possible locations of the singularities of the CGF in the  $\lambda$ -plane. As an example, we depict in Fig. 1 (a) the branch cuts corresponding to continuous singularities of the CGF pertaining to two-terminal transport of noninteracting electrons, Eq. (36) below. This CGF is  $2\pi$ -periodic along the real axis of  $\lambda$ , which guarantees integer values of charge.<sup>12</sup> The branch cuts, depicted by thick lines, are at  $\text{Re } \lambda = (2n - 1)\pi$ , where  $n$  is an integer. The FT ensures that the branch cuts are symmetrically distributed around  $\lambda = i\beta V/2$ , and their positions on the upper positive/negative real and lower negative/positive real sides of the dotted line  $\text{Im } \lambda = \beta V/2$  in Fig. 1 (a) are related. The  $2\pi$ -periodicity is removed by the conformal transformation Eq. (3). Then the branch cuts are on the negative real axis of the  $u$ -plane [Fig. 1 (b)].<sup>26,27,31,32</sup>

The steady-state probability distribution, beyond the central-limit theorem, is derived within the theory of large deviations.<sup>25</sup> At steady state, realized in the  $\tau \rightarrow \infty$  limit, we scale  $q = I\tau$  and  $\mathcal{Z}_\tau \approx e^{\tau \mathcal{I}}$ . Then the integral of the inverse Fourier transform Eq. (4) can be estimated by the saddle-point approximation<sup>48</sup> and the result is written with the rate function<sup>25</sup>  $\mathcal{I}$  as  $P_\tau \approx e^{-\tau \mathcal{I}}$ . Since  $P_\tau$  is real and positive, the saddle point is expected to reside on the imaginary axis of complex  $\lambda$ -plane. Then the rate function is written in the form of a Legendre-Fenchel transform,

$$\mathcal{I}(I) = - \lim_{\tau \rightarrow \infty} \frac{1}{\tau} \ln P_\tau(I\tau) = \max_{\lambda} \{i\lambda I - \mathcal{F}(\lambda)\}. \quad (8)$$

Here  $\lambda$  is a purely imaginary number. In most cases, the CGF is real, i.e. the imaginary part of the exponent of the Fourier integral (4),  $\ln \mathcal{Z}_\tau(\lambda) - i\lambda q$ , is zero on the imaginary axis of  $\lambda$ -plane. Then the imaginary axis is expected to be a steepest path of the integral (4).<sup>48</sup> There are few exceptions where singularities of the CGF are on the imaginary axis<sup>15,16</sup> as we will also find later. The relation between the CGF and the rate function is analogous to that of thermodynamic potentials. It suggests that singularities on the imaginary axis of the  $\lambda$ -plane would also cause characteristic features in the rate function.

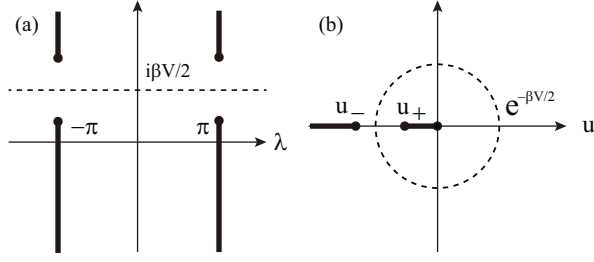


FIG. 1: Singularities of the CGF of noninteracting electrons, Eq. (36), in the  $\lambda$ -plane (a) and in the  $u$ -plane (b). The FT relates the positions of the singularities on the upper positive/negative real and lower negative/positive real sides of the dotted line (a). In  $u$ -plane the FT relates the positions of the singularities inside and outside the dotted circle (b).

### III. MODEL HAMILTONIAN AND CUMULANT-GENERATING FUNCTION

Our explicit calculations are carried out for a simple model [Fig. 2], a single-level quantum dot coupled to a local Einstein phonon, which induces fluctuations in that level.<sup>8–10,49</sup> The model Hamiltonian is

$$\mathcal{H} = \mathcal{H}_{\text{mol}} + \mathcal{H}_{\text{ph}} + \mathcal{H}_{\text{lead}} + \mathcal{H}_{\text{tun},\pm}, \quad (9)$$

where the  $\pm$  subscript is due to the presence of counting fields (see below). The molecular bridge or the atomic wire is described by the Hamiltonian  $\mathcal{H}_{\text{mol}}$ ,

$$\mathcal{H}_{\text{mol}} = [\epsilon_0 + \gamma(b + b^\dagger)]c_0^\dagger c_0, \quad (10)$$

in which  $c_0$  ( $c_0^\dagger$ ) destroys (creates) an electron on the localized level representing the molecule, of energy  $\epsilon_0$ ,  $b$  and  $b^\dagger$  are the destruction and creation operators of the vibrations to which the electron is coupled while residing on the dot, and  $\gamma$  is the strength of the electron-phonon coupling. The vibrational modes obey the harmonic Hamiltonian

$$\mathcal{H}_{\text{ph}} = \omega_0 b^\dagger b, \quad (11)$$

where  $\omega_0$  is the frequency of the Einstein phonon. The leads are represented by free electron gases, of creation and destruction operators  $c_{rk}^\dagger$  and  $c_{rk}$ , and eigen energies  $\epsilon_{rk}$ ,

$$\mathcal{H}_{\text{lead}} = \sum_{r=L,R} \sum_k \epsilon_{rk} c_{rk}^\dagger c_{rk}. \quad (12)$$

Finally there is the tunneling Hamiltonian, coupling the leads to the molecule. This part of the Hamiltonian is augmented by the counting fields. Those appear as phase factors on the operators  $c_{rk}$  and  $c_{rk}^\dagger$ ,

$$\mathcal{H}_{\text{tun},\pm} = \sum_{r=L,R} \sum_k J_r e^{\pm i\lambda_r} c_{rk}^\dagger c_0 + \text{H.c.}, \quad (13)$$

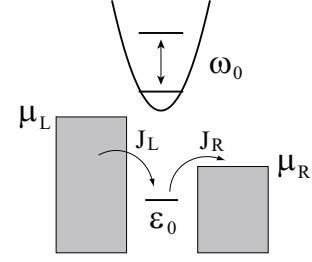


FIG. 2: Schematic description of the single-level quantum dot coupled to an Einstein vibrational mode.

where  $J_L$  and  $J_R$  are the tunneling amplitudes between the left and the right lead, and the dot.

In terms of the tunneling Hamiltonian Eq. (13), the characteristic function is<sup>13</sup>

$$\mathcal{Z}_\tau(\lambda) = \left\langle T_K \exp \left( -i \int_K dt \mathcal{H}_{\text{tun},\pm}(t)_I \right) \right\rangle, \quad (14)$$

where  $K$  denotes the Keldysh contour, which runs from  $t = -\tau/2$  to  $t = \tau/2$  on the upper branch and returns to  $t = -\tau/2$  on the lower one (see Fig. 3) and  $T_K$  is the time-ordering operator along that contour. The superscript  $I$  indicates time dependence in the interaction picture. The  $\pm$  notation indicates the branch of the Keldysh contour on which the tunneling Hamiltonian is effective,  $+$  for the upper branch in Fig. 3 and  $-$  for the lower one. In the long-time limit, the scaled CGF depends only on the difference of the two counting fields

$$\lambda = \lambda_L - \lambda_R. \quad (15)$$

As  $\lambda_L + \lambda_R$  counts the number of electrons flowing into the dot, the fact that the CGF depends solely on  $\lambda$  implies current conservation.

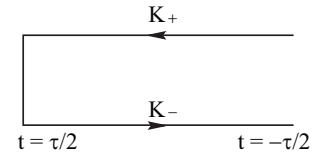


FIG. 3: The Keldysh contour.

The FT, including current conservation as represented by Eq. (15), has been proved using the perturbation expansion in the interaction.<sup>36</sup> Although the proof was for Coulomb interaction case, it may be extended to the electron-phonon interaction case as well. We even expect it to be correct for any closed diagram in the linked-cluster expansion (for example, the diagrams in Fig. 4) which suggests, in turn, that by simply summing up closed diagrams one will obtain an approximate generating function satisfying the FT and current conservation.

To carry out the perturbation expansion in the present case, we utilize the nonequilibrium Luttinger-Ward potential,<sup>45–47,50</sup>  $\Phi$ . This theory relies on the self energy

of the Green function and requires self-consistent calculations to ensure various conservation laws. For our case, since the electron-phonon coupling  $\gamma$  is weak, we perform the calculation up to second-order accuracy  $\mathcal{O}(\gamma^2)$  (see Appendix A for details)

$$\mathcal{F}(\lambda) = \mathcal{F}_0(\lambda) - \bar{\Phi}^{(2)}(\lambda), \quad (16)$$

where  $\mathcal{F}_0$  is the CGF pertaining to noninteracting electrons, and is given in terms of the Keldysh Green function  $g_\lambda$  of the *electronic* part of the Hamiltonian Eq. (9),

$$\mathcal{F}_0(\lambda) = \frac{1}{2\pi} \int d\omega \ln \det[g_\lambda^{-1}(\omega)], \quad (17)$$

where the trace is performed over the  $2 \times 2$  Keldysh space. The scaled Luttinger-Ward potential,  $\bar{\Phi}^{(2)}$ , appearing in Eq. (16) is accurate up to  $\mathcal{O}(\gamma^2)$ ,

$$\lim_{\tau \rightarrow \infty} \frac{1}{\tau} \Phi(g_\lambda) = \bar{\Phi}(\lambda) = \bar{\Phi}^{(2)}(\lambda) + \mathcal{O}(\gamma^4). \quad (18)$$

Here is a subtle point. A naive second-order perturbation theory is not capable of producing the correct nonequilibrium phonon distribution,<sup>6,7,19,51</sup> as has been recognized before for a local moment coupled with a nonequilibrium electron gas.<sup>52</sup> Therefore, we will first perform a re-summation of linked diagrams for the cumulant-generating function, which is known to suffice for a proper description of the steady state,<sup>17</sup> and then calculate accurately within second order in the electron-phonon coupling.

### A. The Electronic part

The inverse Keldysh Green function  $g_\lambda$  reads

$$g_\lambda(\omega)^{-1} = \begin{bmatrix} \omega - \epsilon_0 + i \sum_{r=L,R} \Gamma_r [f_r^-(\omega) - f_r^+(\omega)]/2 & i \sum_{r=L,R} \Gamma_r f_r^+(\omega) e^{i\lambda_r} \\ -i \sum_{r=L,R} \Gamma_r f_r^-(\omega) e^{-i\lambda_r} & -\omega + \epsilon_0 + i \sum_{r=L,R} \Gamma_r [f_r^-(\omega) - f_r^+(\omega)]/2 \end{bmatrix}, \quad (19)$$

where  $\Gamma_L$  and  $\Gamma_R$  are the partial widths of the localized level induced by the coupling with the leads,

$$\Gamma_r = 2\pi\nu_r |J_r|^2, \quad r = L, R. \quad (20)$$

Here  $\nu_L$  and  $\nu_R$  are the densities of states in the left and right leads. Each of the leads is specified by its chemical potential  $\mu_r$ , such that  $\mu_L - \mu_R = V$ , and their electron/hole distribution is accordingly given by

$$f_r^\pm(\omega) = \frac{1}{e^{\pm\beta(\omega - \mu_r)} + 1}. \quad (21)$$

The Green function itself is then

$$g_\lambda(\omega) = \begin{bmatrix} g_\lambda^{++}(\omega) & g_\lambda^{+-}(\omega) \\ g_\lambda^{-+}(\omega) & g_\lambda^{--}(\omega) \end{bmatrix}, \quad (22)$$

and its four components are

$$g_\lambda^{ss}(\omega) = \frac{1}{\Omega_\lambda(\omega)} \left( \frac{1}{s(\omega - \epsilon_0) + i\Gamma/2} + is \sum_{r=L,R} g_r^{s\bar{s}}(\omega) \right), \quad (23)$$

$$g_\lambda^{s\bar{s}}(\omega) = \sum_{r=L,R} \frac{g_r^{s\bar{s}}(\omega)}{\Omega_\lambda(\omega)} e^{is\lambda_r},$$

where  $\bar{s} = -/+$  for  $s = +/-$ . The lesser and greater Green functions, in the absence of the counting field,  $g_r^{s\bar{s}}$ , are expressed with the density of states on the localized

level normalized by  $\Gamma = \sum_{r=L,R} \Gamma_r$ , the width of the resonance on the localized level,

$$\bar{\rho}(\omega) = \frac{\Gamma^2/4}{(\omega - \epsilon_0)^2 + \Gamma^2/4}, \quad (24)$$

as

$$g_r^{\pm\mp}(\omega) = \pm 4i \frac{\Gamma_r}{\Gamma^2} \bar{\rho}(\omega) f_r^\pm(\omega). \quad (25)$$

The dependence on the counting field is contained in the function  $\Omega_\lambda$ ,

$$\Omega_\lambda(\omega) = -\frac{\det g_\lambda(\omega)^{-1}}{\det g_0(\omega)^{-1}} = 1 + \mathcal{T}(\omega) \times [f_L^+(\omega) f_R^-(\omega) (e^{i\lambda} - 1) + f_R^+(\omega) f_L^-(\omega) (e^{-i\lambda} - 1)]. \quad (26)$$

Here appears the frequency-dependent transmission of the localized level,

$$\mathcal{T}(\omega) = \alpha \bar{\rho}(\omega), \quad (27)$$

with the transmission probability at resonance,

$$\alpha = \frac{4\Gamma_L \Gamma_R}{\Gamma^2}. \quad (28)$$

Our calculation is confined to the extended wide-band limit,<sup>19</sup> in which the level broadening  $\Gamma$  or the dot level

$|\epsilon_0|$  is larger than all other energy scales including the phonon frequency  $\omega_0$ , i. e.

$$|V|, k_B T, \omega_0 \ll \Gamma, \quad (29)$$

or

$$|V|, k_B T, \omega_0, \Gamma \ll |\epsilon_0|. \quad (30)$$

With this condition, the frequency-dependent normalized density of states Eq. (24) is replaced by its value at the Fermi energy,

$$\bar{\rho}(\omega) \approx \rho_0 = \frac{\Gamma^2}{4\epsilon_0^2 + \Gamma^2}. \quad (31)$$

Within the extended wide-band limit approximation the transmission becomes energy independent, and consequently the computation of the integral determining the zeroth-order CGF [see Eq. (17)] is straightforward. The key observation is that the variable transformation  $z = \exp[\beta(\omega' + (\mu_L + \mu_R)/2)]$  transforms Eq. (26) into a simpler form,

$$\Omega_\lambda(\omega') = \frac{(z - Z_{\lambda+})(z - Z_{\lambda-})}{(1 + z e^{-\beta(\mu_L + \mu_R)/2})(1 + z e^{\beta(\mu_L + \mu_R)/2})}, \quad (32)$$

where

$$Z_{\lambda\pm} = X_\lambda \pm \sqrt{X_\lambda^2 - 1} \quad (33)$$

and

$$X_\lambda = (\mathcal{T} - 1) \cosh \frac{\beta V}{2} - \mathcal{T} \cosh \frac{\beta V + 2i\lambda}{2}. \quad (34)$$

Then we obtain

$$\frac{\partial \mathcal{F}_0(\lambda)}{\partial(i\lambda)} = \frac{-1}{2\pi\beta} \frac{2\partial_{i\lambda} X_\lambda}{Z_{\lambda+} - Z_{\lambda-}} \ln \frac{Z_{\lambda-}}{Z_{\lambda+}}, \quad (35)$$

and consequently the CGF itself is derived<sup>12</sup> from Eq. (35) by integrating over  $\lambda$ ,

$$\mathcal{F}_0(\lambda) = \frac{(\text{arccosh} X_\lambda)^2}{2\pi\beta} - \frac{\beta V^2}{8\pi}. \quad (36)$$

The counting field dependence is only through  $X_\lambda$ . This result obeys the FT since when  $\lambda \rightarrow -\lambda + i\beta V$ ,  $X_\lambda$  is unchanged. Actually, already in Eqs. (17) and (26) we can see the FT is satisfied since

$$\Omega_{-\lambda+i\beta V}(\omega) = \Omega_\lambda(\omega). \quad (37)$$

This CGF possesses continuous lines of singularities for  $X_\lambda \in [1, \infty)$ . As discussed in Sec. II, in the  $u$ -plane these become branch cuts  $(-\infty, u_-]$  and  $[u_+, 0)$ , where the branch points are at  $u_\pm = e^{-\beta V/2}(x \pm \sqrt{x^2 - 1})$ , with  $x = \cosh(\beta V/2)(1 - 1/\mathcal{T}) - 1/\mathcal{T}$  [see Figs. 1 (a) and (b)]. The zeroth-order CGF (36) takes a particular simple form for a symmetric bridge  $\Gamma_L = \Gamma_R$  at resonance

$\epsilon_0 = 0$ , for which the transmission is perfect  $\mathcal{T} = 1$  [see Eqs. (27), (28), and (31)]

$$\mathcal{F}_0(\lambda) = i\lambda(V + i\lambda/\beta)/(2\pi), \quad (38)$$

which describes Gaussian thermal fluctuations. On the other hand, when the bridge is extremely askew,  $\Gamma_R \ll \Gamma_L$  or  $|\epsilon_0| \gg \Gamma$  and thus  $\mathcal{T} \ll 1$  one may expand the CGF to obtain

$$\mathcal{F}_0(\lambda) \approx \frac{\mathcal{T}V}{2\pi} \left( \frac{e^{i\lambda} - 1}{1 - e^{-\beta V}} + \frac{e^{-i\lambda} - 1}{e^{\beta V} - 1} \right), \quad (39)$$

which is the bi-directional Poisson form.

## B. The phonon-induced part

The nonequilibrium Luttinger-Ward functional  $\Phi$  in Eq. (18) results from the coupling of the charge carriers to the vibrational modes, and therefore it is a functional of the Keldysh phonon Green function,

$$d_\lambda(\omega) = \begin{bmatrix} d_\lambda^{++}(\omega) & d_\lambda^{+-}(\omega) \\ d_\lambda^{-+}(\omega) & d_\lambda^{--}(\omega) \end{bmatrix}, \quad (40)$$

whose four components are

$$\begin{aligned} d^{\pm\pm}(\omega) &= \text{Re} \frac{2\omega_0}{(\omega + i0^+)^2 - \omega_0^2} \\ &\quad - i\pi \coth \frac{\beta\omega}{2} [\delta(\omega - \omega_0) - \delta(\omega + \omega_0)], \\ d^{\mp\pm}(\omega) &= -2\pi i [\delta(\omega - \omega_0) - \delta(\omega + \omega_0)] n^\mp(\omega). \end{aligned} \quad (41)$$

Here  $0^+$  is a positive infinitesimal, and  $n^\pm$  is the Bose distribution

$$n^\pm(\omega) = \pm \frac{1}{e^{\pm\beta\omega} - 1}. \quad (42)$$

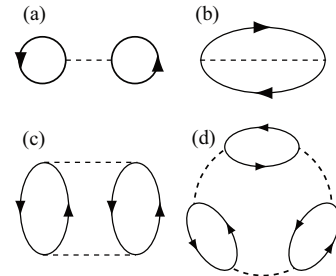


FIG. 4: Second-order diagrams, the Hartree (a) and Fock (b) terms. Diagram (c) is one of the fourth-order ones, and diagram (d) is one of sixth-order diagrams (a ring diagram). The full lines denote electron propagators, and the dashed ones phonon propagators.

The functional  $\Phi$  can be expanded diagrammatically in powers of the electron-phonon coupling [see Appendix A



for more details], or more precisely, in the small parameter

$$g = \frac{2\gamma^2}{\pi\Gamma^2}. \quad (43)$$

Figure 4 shows the second-order diagrams [(a) and (b)] and two of higher-order diagrams [(c) and (d)]. Diagram (a) represents the Hartree term, Eq. (A15), which is ignored below since it is independent of the phonon distribution. Diagram (b) represents the Fock term, Eq. (A20), which depends on the Bose distribution. The actual nonequilibrium phonon distribution function can be obtained only by summing over infinite-order (in the electron-phonon coupling) diagrams. Therefore we

carry out a re-summation of particular diagrams in the random-phase approximation (RPA) [see the discussion in Appendix A and Eq. (A21)]

$$\bar{\Phi}^{\text{RPA}}(g_\lambda) = \frac{1}{4\pi} \int d\omega \ln \det D_\lambda(\omega)^{-1}, \quad (44)$$

and then calculate up to second-order accuracy

$$\bar{\Phi}^{\text{RPA}}(g_\lambda) = \bar{\Phi}^{(2)}(\lambda) + \mathcal{O}(g^2). \quad (45)$$

Here our expectation is that RPA would provide accurate result up to second order in  $\gamma$  [see Eq. (18)] except for the Hartree term, which we ignore. The dressed phonon Green function  $D_\lambda$  is

$$D_\lambda(\omega)^{-1} = d(\omega)^{-1} - \tau_3 \Pi_\lambda(\omega) \tau_3 = \begin{bmatrix} (\omega^2 - \omega_0^2)/2\omega_0 - \Pi_\lambda^{++}(\omega) & \Pi_\lambda^{+-}(\omega) \\ \Pi_\lambda^{-+}(\omega) & -(\omega^2 - \omega_0^2)/2\omega_0 - \Pi_\lambda^{--}(\omega) \end{bmatrix}, \quad (46)$$

with  $\tau_3$  being the third Pauli matrix

$$\tau_3 = \begin{bmatrix} 1 & 0 \\ 0 & -1 \end{bmatrix}. \quad (47)$$

In Eq. (46) appears the Keldysh particle-hole propagator  $\Pi$ , whose lesser/greater components are given by

$$\begin{aligned} i\Pi_\lambda^{\pm\mp}(\omega) &= \frac{\gamma^2}{2\pi} \int d\omega' g_\lambda^{\pm\mp}(\omega' + \omega/2) g_\lambda^{\mp\pm}(\omega' - \omega/2) \\ &= \sum_{r,r'=L,R} i\tilde{\Pi}_{rr'\lambda}^{\pm\mp}(\omega) e^{\pm i(\lambda_r - \lambda_{r'})}, \end{aligned} \quad (48)$$

where

$$i\tilde{\Pi}_{rr'\lambda}^{\pm\mp}(\omega) = \frac{\gamma^2}{2\pi} \int d\omega' \frac{g_r^{\pm\mp}(\omega' + \omega/2) g_{r'}^{\mp\pm}(\omega' - \omega/2)}{\Omega_\lambda(\omega' + \omega/2) \Omega_\lambda(\omega' - \omega/2)}. \quad (49)$$

(See Appendix B for more details.) The particle-hole propagator satisfies the relations

$$\begin{aligned} \Pi_\lambda^{+-}(\omega) &= \Pi_\lambda^{-+}(-\omega), \\ \tilde{\Pi}_\lambda^{+-}(\omega) &= \tilde{\Pi}_\lambda^{-+}(-\omega), \end{aligned} \quad (50)$$

with  $\tilde{\Pi}_\lambda^{+-}(\omega) = \sum_{rr'} \tilde{\Pi}_{rr'\lambda}^{+-}(\omega)$ . The analytic expression of Eq. (49) in the extended wide-band limit is lengthy and is given by Eq. (B3). For  $\lambda = 0$  it attains a simple form

$$i\tilde{\Pi}_{rr'0}^{+-}(\omega) \approx g\alpha_{rr'}\rho_0 \frac{\mu_r - \mu_{r'} - \omega}{e^{\beta(\mu_r - \mu_{r'} - \omega)} - 1}, \quad (51)$$

with

$$\alpha_{rr'} = 4\Gamma_r \Gamma_{r'} / \Gamma^2. \quad (52)$$

Relegating detailed derivations to Appendix B, the causal and anti-causal components obey

$$\Pi_\lambda^{++}(\omega) + \Pi_\lambda^{--}(\omega) = \tilde{\Pi}_\lambda^{+-}(\omega) + \tilde{\Pi}_\lambda^{-+}(\omega) + \phi_\lambda^S(\omega), \quad (53)$$

$$\Pi_\lambda^{++}(\omega) - \Pi_\lambda^{--}(\omega) = 2\text{Re}\Pi^R(\omega) + \phi_\lambda^A(\omega). \quad (54)$$

The definition of  $\phi_\lambda^S$  and its analytic expression in the extended wide-band limit are given in Eq. (B7) and Eqs. (B10) and (B11), respectively. One finds that  $\phi_\lambda^S$  is even in  $\omega$ . It turns out that  $\phi_\lambda^A$  may be safely neglected [see Eq. (B15)].

Finally, the retarded component is given by exploiting the Kramers-Kronig relation

$$\Pi^R(\omega) = \frac{i}{2\pi} \int d\omega' \frac{\Pi_0^{+-}(\omega') - \Pi_0^{+}(\omega')}{\omega - \omega' + i0^+}. \quad (55)$$

The particle-hole propagator is proportional to the small parameter  $g$ , Eq. (43).

Having determined the dressed phonon Green function Eq. (46), we now use it to obtain  $\bar{\Phi}^{\text{RPA}}$ , Eq. (44). It is expedient to calculate its derivative with respect to  $\lambda$ . By presenting the determinant of the dressed phonon Green function in the form [using Eqs. (53) and (54)]

$$-\det D_\lambda^{-1}(\omega) = \left( \frac{\omega^2 - \omega_0^2}{2\omega_0} - \text{Re}\Pi^R(\omega) \right)^2 + \mathcal{A}_\lambda(\omega), \quad (56)$$

where

$$\begin{aligned} \mathcal{A}_\lambda(\omega) &= \Pi_\lambda^{+-}(\omega) \Pi_\lambda^{+}(\omega) \\ &\quad - \frac{1}{4} [\tilde{\Pi}_\lambda^{+-}(\omega) + \tilde{\Pi}_\lambda^{+}(\omega) + \phi_\lambda^S(\omega)]^2, \end{aligned} \quad (57)$$

we obtain

$$\frac{\partial \bar{\Phi}^{\text{RPA}}(g_\lambda)}{\partial \lambda} = \int \frac{d\omega}{4\pi} \frac{\partial_\lambda \mathcal{A}_\lambda(\omega)}{\left(\frac{\omega^2 - \omega_0^2}{2\omega_0} - \text{Re}\Pi^R(\omega)\right)^2 + \mathcal{A}_\lambda(\omega)}. \quad (58)$$

The integral here is carried out to leading order in  $g$ . The integrand has four poles, which within that accuracy are given by

$$\pm[\omega_0 + \text{Re}\Pi^R(\omega_0)] \pm i\sqrt{\mathcal{A}_\lambda(\omega_0)}, \quad (59)$$

where we have used  $\mathcal{A}_\lambda(\omega) = \mathcal{A}_\lambda(-\omega)$ .

The locations of poles of the integrand in Eq. (58) are complex functions of  $\lambda$ . Consider them first in the limit  $\lambda \rightarrow 0$ . Since

$$\begin{aligned} \mathcal{A}_0(\omega_0) &= \left( \frac{1}{2} \sum_{r,r'=L,R} g\alpha_{rr'}\rho_0^2(\omega_0 - \mu_r + \mu_{r'}) \right)^2 \\ &= (2g\rho_0^2\omega_0)^2, \end{aligned} \quad (60)$$

is a positive real number, then at small enough  $\lambda$ , the real part of the square root satisfies  $\text{Re}\sqrt{\mathcal{A}_\lambda(\omega_0)} > 0$  and thus the integration yields

$$\frac{\partial \bar{\Phi}^{\text{RPA}}(g_\lambda)}{\partial \lambda} \approx \partial_\lambda \sqrt{\mathcal{A}_\lambda(\omega_0)}, \quad (61)$$

up to  $\mathcal{O}(g)$ . It follows that

$$\bar{\Phi}^{(2)}(\lambda) = \sqrt{\mathcal{A}_\lambda(\omega_0)} - 2g\rho_0^2\omega_0, \quad (62)$$

which satisfies the normalization condition  $\bar{\Phi}^{(2)}(0) = 0$ . Away from the origin  $\lambda = 0$ ,  $\text{Re}\sqrt{\mathcal{A}_\lambda(\omega_0)}$  may be negative. When this is the case we obtain

$$\bar{\Phi}^{(2)}(\lambda) = -\sqrt{\mathcal{A}_\lambda(\omega_0)} - 2g\rho_0^2\omega_0. \quad (63)$$

Hence a branch cut appears at  $\lambda$  satisfying  $\text{Re}\sqrt{\mathcal{A}_\lambda(\omega_0)} = 0$ .

In order to carry out a large-deviation analysis it suffices to consider the imaginary axis of the  $\lambda$ -plane, since there the rate function (8) is real. On the imaginary axis,  $\mathcal{A}_\lambda(\omega_0)$  is a real function. When  $\mathcal{A}_\lambda(\omega_0) > 0$  the imaginary part of  $\bar{\Phi}^{(2)}$  is zero and thus the imaginary axis can serve as the steepest path<sup>48</sup> of the integral Eq. (4). When  $\mathcal{A}_\lambda(\omega_0) \leq 0$ , there appears a branch cut on the imaginary axis. One might have thought that the branch cut would be detrimental to the saddle-point approximation of the integral in Eq. (4). Here we point out that a complex integration along a path encircling the branch cut oscillates rapidly in the  $\tau \rightarrow \infty$  limit and thus would be averaged out. Therefore we will neglect the contribution from the branch cut.

Equations (62) and (63) are the main results of this paper. Similar expressions have been reached by Haupt *et al.* in Refs. 19; these authors concentrated on the first few cumulants. Here we obtain analytical expressions for

the CGF; those enable us to examine its singularities and to fully analyze the rate function itself, as is detailed in the next Section.

Finally, we verify that our results obey the FT. Exploiting the detailed-balance relation,

$$\tilde{\Pi}_{rr' - \lambda + i\beta V}^{+}(\omega) = \tilde{\Pi}_{rr' \lambda}^{-+}(\omega) = \tilde{\Pi}_{rr' \lambda}^{+-}(\omega)e^{\beta(\omega - \mu_r + \mu_{r'})}, \quad (64)$$

and the relations

$$\begin{aligned} \Pi_{-\lambda + i\beta V}^{+}(\omega) &= \Pi_{\lambda}^{+-}(\omega)e^{\beta\omega}, \\ \tilde{\Pi}_{-\lambda + i\beta V}^{+}(\omega) &= \tilde{\Pi}_{\lambda}^{+-}(\omega), \\ \phi_{-\lambda + i\beta V}^S(\omega) &= \phi_{\lambda}^S(\omega), \end{aligned} \quad (65)$$

we find

$$\mathcal{A}_{-\lambda + i\beta V}(\omega) = \mathcal{A}_\lambda(\omega). \quad (66)$$

Therefore Eqs. (62) and (63) satisfy the FT,

$$\bar{\Phi}^{(2)}(-\lambda + i\beta V) = \bar{\Phi}^{(2)}(\lambda). \quad (67)$$

#### IV. RESULTS AND DISCUSSION

In the following we confine ourselves to a symmetric junction,  $\alpha = 1$  ( $\Gamma_L = \Gamma_R$ ), and thus the normalized density of states on the dot at the Fermi level dominates the transmission probability,  $\mathcal{T} = \rho_0$  [see Eqs. (24), (27), (28), and (31)]. The numerical results are all obtained for the electron-phonon coupling constant, Eq. (43),  $g = 0.1$ , unless otherwise specified.

##### A. Average current and noise

Figure 5 (a) shows the source-drain bias voltage dependence of the current  $\langle\langle I \rangle\rangle$  at a finite temperature  $\beta\omega_0 = 10$  (solid lines) and at zero temperature (dashed lines) for a perfect,  $\mathcal{T} = 1$ , and a relatively weak,  $\mathcal{T} = 0.5$ , transmission probabilities. At perfect transmission the current is suppressed above the threshold,  $|V| > \omega_0$ , because electrons are inelastically backscattered by phonons. When the transmission is weak,  $\mathcal{T} = 0.5$ , the current is slightly enhanced above the threshold. These results are consistent with previous ones.<sup>19</sup> A finite temperature tends to smear the kink structure of the  $\mathcal{T} = 1$  curve; it affects far less the average current at weak transmission,  $\mathcal{T} = 0.5$ , where the solid and dashed lines almost overlap.

Figure 5 (b) depicts the current noise  $\langle\langle I^2 \rangle\rangle$ . At perfect transmission the noise is absent below the threshold  $|V| < \omega_0$  at zero temperature. Thermal fluctuations which arise at finite temperatures induce additional noise below the threshold. Although the current is suppressed above the threshold  $|V| = \omega_0$  by the inelastic phonon scattering, the noise is significantly enhanced. This indicates that inelastic phonon scattering broadens

the probability distribution of the current. In the case of a weak transmission,  $\mathcal{T} = 0.5$ , the temperature effect is less dramatic—the noise is simply enhanced.

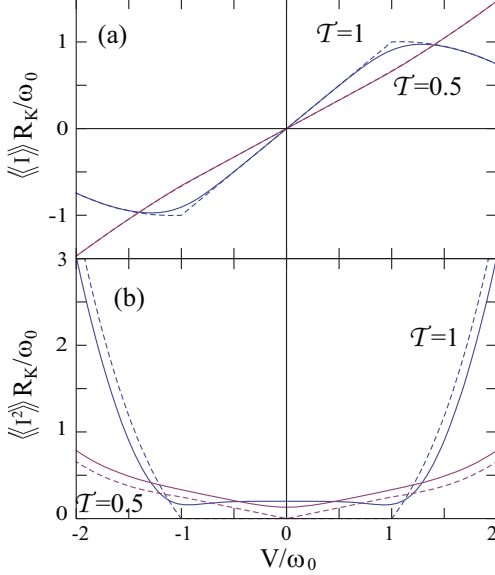


FIG. 5: The source-drain bias voltage dependence of the current (a) and the current noise (b) for  $\mathcal{T} = 1$  and 0.5. Solid lines— $\beta\omega_0 = 10$ ; dashed lines—zero temperature. The vertical axes are normalized by  $\omega_0/R_K$ , where  $R_K = 2\pi$  is the resistance quantum.

## B. Singularities and the rate function

At zero temperature, it is possible to obtain a simpler form for the scaled CGF, which is useful for finding its singularities. For positive voltages  $V \geq 0$ , the explicit form of the electronic part of the CGF, Eq. (36), reads

$$\mathcal{F}_0(\lambda) = \frac{V}{2\pi} \ln \tilde{u}, \quad \tilde{u} = 1 + \mathcal{T}(u - 1), \quad (68)$$

where  $u$  is defined in Eq. (3). The function  $\mathcal{A}_\lambda$  which determines the phonon part is given by

$$\mathcal{A}_\lambda(\omega_0) = 4g^2\mathcal{T}^2[(1 - 1/\tilde{u})(\mathcal{T} - 1)V + \mathcal{T}\omega_0]^2, \quad (69)$$

for  $0 < V < \omega_0$  and

$$\begin{aligned} \mathcal{A}_\lambda(\omega_0) = & g^2\mathcal{T}^2\{[V(1 - \mathcal{T} + \tilde{u}^2(2\mathcal{T} - 1)) + (\mathcal{T} - 1 \\ & + \tilde{u}(2 - \tilde{u} + 2\mathcal{T}(\tilde{u} - 1)))\omega_0]^2 - u\mathcal{T}^2(V \\ & - \omega_0)[2\tilde{u}\omega_0 + u(V + (2\tilde{u} - 1)\omega_0)]\}/\tilde{u}^4, \end{aligned} \quad (70)$$

for  $V \geq \omega_0$ . Below, we investigate the analytic properties of the phonon-induced part of the CGF.

### 1. Elastic phonon scattering

As at zero temperature phonons cannot be excited when  $0 < V < \omega_0$ , and electron transport at such volt-

ages is hence affected only by *elastic* phonon scattering. Figure 6 (a) shows schematically the square-root branch cut of  $\tilde{\Phi}^{(2)}$ , Eqs. (62) and (63). We find that the  $u$ -plane is separated into two by the branch cut. This branch cut intersects the real axis at  $u_0 = 1 - 1/\mathcal{T}$  [ $u_0$  is indicated by empty dots in Fig. 6 (a)] and  $u_1 = (\mathcal{T} - 1)(V + \omega_0)/[V(\mathcal{T} - 1) + \mathcal{T}\omega_0]$ . Around these points,  $\mathcal{A}_\lambda$  can be expanded as

$$\mathcal{A}_\lambda \approx g^2 \frac{4V^2(\mathcal{T} - 1)^2}{(u - u_0)^2}, \quad (71)$$

$$\mathcal{A}_\lambda \approx g^2 \frac{4\mathcal{T}^4(\mathcal{T}\omega_0 + (\mathcal{T} - 1)V)^4}{V^2(\mathcal{T} - 1)^2}(u - u_1)^2. \quad (72)$$

Upon sweeping the transmission  $\mathcal{T}$  from 0 to 1,  $u_0$  increases from  $-\infty$  to 0, while  $u_1$  increases but at  $\mathcal{T}_C = V/(V + \omega_0)$  jumps from  $+\infty$  to  $-\infty$ . Accordingly, we may define two regimes, or phases<sup>28</sup>, I ( $\mathcal{T} < \mathcal{T}_C$ ) and II ( $\mathcal{T} > \mathcal{T}_C$ ) as indicated in Fig. 6 (a). This classification roughly captures the behavior of the average current and the current noise. Figures 6 (b) and (c) depict the corrections induced by the electron-phonon interaction in the average current and in the current noise, respectively,

$$\langle\langle I^n \rangle\rangle_{\text{ph}} = \frac{\partial^n \tilde{\Phi}^{(2)}}{\partial (i\lambda)^n} \Big|_{\lambda=0}. \quad (73)$$

We find that the electron-phonon interaction always increases the average current under the conditions adopted here [Fig. 6 (b)]. On the other hand, the noise can be either enhanced or suppressed, depending on which regime the transmission is in [Fig. 6 (c)].

In regime I, one of the intersection points,  $u_1$ , is on the positive real axis, outside the unit circle  $|u| = 1$  [the left panel of Fig. 6 (a)]. Therefore, in the  $\lambda$ -plane, there is a nonanalytic point on the positive  $i\lambda$ -axis, which induces a weak non-convexity of the CGF as shown in Fig. 7 (a) [The non-convex region is indicated by an arrow in Fig. 7 (a). For comparison, we also plot the  $g = 0$  case for which the CGF is convex, shown by the dotted line.]. Figure 7 (b) exhibits the rate function, the Legendre transform of the CGF, Eq. (8). The rate function is multi-valued around  $I/\langle I \rangle_0 \sim 3$  (the thick line in the figure) because of the non-convexity of the CGF. As seen from its definition Eq. (8), the rate function is obtained by choosing the  $\lambda$  that maximizes the expression in the curly brackets there. Then, similar to the way a first-order phase transition manifests itself in thermodynamics, a kink appears in the rate function. We note that the location of the kink does not coincide with that of the peak; the peak of the rate function is at  $\lambda = 0$  where  $\mathcal{I} = 0$  and  $I = \langle I \rangle$ . The physical consequence is that the elastic phonon scattering broadens the probability distribution by enhancing the probability to observe currents larger than the average value. The kink is a consequence of the non-convexity of the CGF on the positive real axis of the  $u$ -plane, a feature which is absent in the noninteracting electron case, and is a signature of the electron-phonon correlation.



In regime II the two intersection points are on the negative real axis of the  $u$ -plane [the right panel of Fig. 6 (a)]. In this case, the CGF can be reduced to that of non-interacting electron transport.<sup>26</sup> The CGF and the rate function pertaining to this case are plotted in Figs. 7 (c) and (d). The CGF is convex and the corresponding rate function is concave. In this regime the peak position is shifted from that for  $g = 0$  [dashed line]. The elastic scattering by the phonons can either broaden or shrink the width of the rate function depending on the transmission probability as we deduce from Fig. 6 (c).

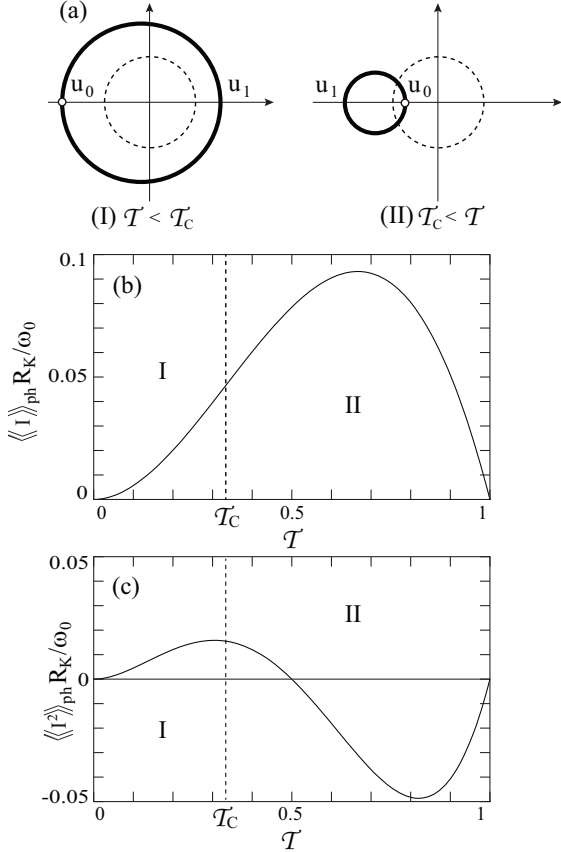


FIG. 6: (a) Schematic picture of the branch cut of  $\bar{\Phi}^{(2)}$  in the complex  $u$ -plane below threshold,  $0 < V < \omega_0$ . The dashed circles are the unit ones. The corrections induced by elastic electron-phonon scattering to the average current and the current noise are portrayed in panel (b) and (c), respectively. The bias voltage is  $V/\omega_0 = 0.5$ . See text for the significance of  $\mathcal{T}_C$ .

## 2. Inelastic phonon scattering

Above threshold  $V \geq \omega_0$ , the inelastic phonon scattering becomes possible. The analytic properties of the scaled CGF in this regime depend on the bias voltage. The branch cuts in the  $u$ -plane are schematically shown in Fig. 8 (a). Three branch points,  $u_1$ ,  $u_2$ , and  $u_3$  can be obtained by searching for the roots of  $\mathcal{A}_\lambda(u) = 0$  [the

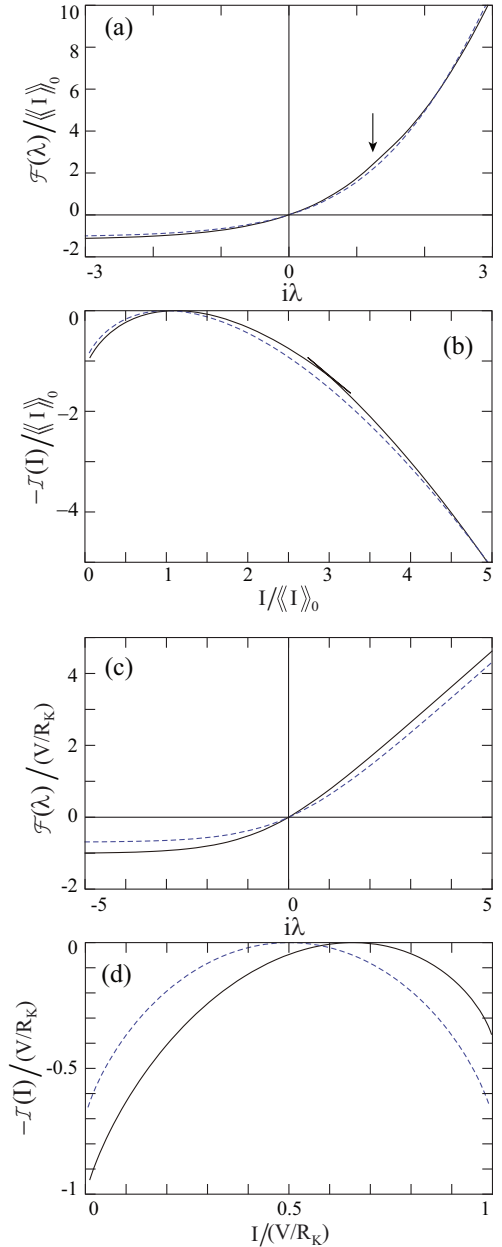


FIG. 7: The scaled CGF (a) and the rate function (b) in regime I ( $\mathcal{T} = 0.1$ ). Solid lines are for  $g = 0.1$  and dashed lines are for  $g = 0$ . The bias voltage is below threshold,  $V/\omega_0 = 0.5$ . The CGF is plotted as a function of the counting field on the imaginary axis. The axes are normalized by  $\langle\langle I \rangle\rangle_0 = \mathcal{T}V/R_K$ . The scaled CGF (c) and the rate function (d) in regime II ( $\mathcal{T} = 0.5$ ).

filled dots in Fig. 8 (a)]. In addition there is another point,  $u_0 = 1 - 1/\mathcal{T}$  [the empty dots in Fig. 8 (a)], around which  $\mathcal{A}_\lambda$  can be expanded

$$\mathcal{A}_\lambda \approx g^2 \frac{2V(\mathcal{T} - 1)(\omega_0 - V)}{\mathcal{T}(u - u_0)^3}. \quad (74)$$

The branch point  $u_1$  is always on the negative real axis such that  $u_1 \leq u_0$ . From the positions of the other two

branch points,  $u_2$  and  $u_3$ , we identify three regimes, see Fig. 8 (a). In regime I the two branch points are on the positive real axis outside the unit circle [dashed circles in Fig. 8 (a) are unit circles]. As  $\mathcal{T}$  increases  $u_2$  and  $u_3$  approach one another and meet at  $\mathcal{T} = \mathcal{T}_-$ . Then in regime II, the two branch points are located symmetrically off the real axis. Upon further increasing  $\mathcal{T}$ ,  $u_2$  and  $u_3$  move in the complex plane and at  $\mathcal{T} = \mathcal{T}_+$  they meet on the real axis again. In regime III, the two branch points are on the positive real axis inside the unit circle.

In Figs. 9 (a) and (b) we plot the CGF and the rate function pertaining to regime I. The overall tendencies are similar to those found in regime I below threshold,  $0 < V < \omega_0$ . In the shaded area of Fig. 9 (a) the CGF is nonanalytic and non-convex. This gives rise to a stronger kink structure in the rate function [Fig. 9 (b)]. Figures 9 (c) and (d) present the CGF and the rate function in regime II. The overall tendency is again similar to those of regime II below threshold. However, because of the non-analyticities off the real axis, the statistics would not be reduced to that of noninteracting electrons.

We note that our identification of the three regimes roughly captures the behavior of the corrections to the current and the noise induced by the electron-phonon interaction [Figs. 8 (b) and (c)], which oscillate as a function of the transmission probability.<sup>5,20</sup>

### C. Fluctuation theorem

The analysis of the CGF and the rate function in regime III [see Fig. 8] is rather subtle. At zero temperature, there develops a non-convex region in the CGF, and the origin  $\lambda = 0$  might enter it. When this happens, second-order perturbation fails since the rate function does not satisfy the relation  $\mathcal{I}(I = \langle I \rangle) = 0$  [this relation is related to the normalization condition  $\mathcal{F}(\lambda = 0) = 0$ ]. We therefore study regime III at finite temperatures, taking as an example  $\beta\omega_0 = 10$ , and show that the FT is crucial for obtaining a physically reasonable result. Note that when the symmetry (7) holds, the FT (6) is also preserved within the large-deviation analysis,<sup>54</sup>

$$\begin{aligned} \mathcal{I}(I) &= \max_{\xi} \{ \xi I - \mathcal{F}(i\xi + i\beta V) \} \\ &= \max_{\xi^*} \{ -\xi^* I - \beta IV - \mathcal{F}(-i\xi^*) \} \\ &= \mathcal{I}(-I) - \beta IV. \end{aligned} \quad (75)$$

Figure 10 exhibits the CGF and the rate function at perfect transmission. For comparison, we plot the corresponding curves for noninteracting electrons, Eq. (38) [dashed lines]. As we have already noted when discussing the current noise, Fig. 5 (b), the width of the rate function is enhanced by inelastic phonon scattering [Fig. 10 (b)]. The CGF obeys the FT, Eq. (7), and the curves are symmetric around the dot-dashed vertical line at  $i\lambda = -\beta V/2$  [Fig. 10 (a)]. The peak of the

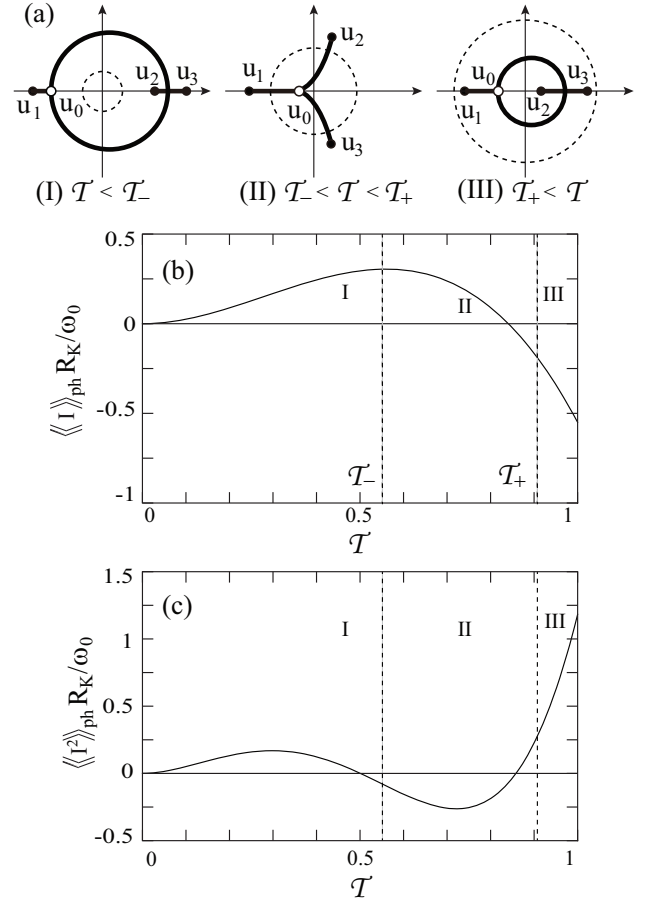


FIG. 8: (a) Schematic picture of the branch cut of  $\bar{\Phi}^{(2)}$  in the complex  $u$ -plane above threshold  $V > \omega_0$ . The dashed circles are the unit ones. (b) The corrections induced by the electron-phonon coupling to the current and (c) to the current noise. The bias voltage is  $V/\omega_0 = 1.5$ . The boundaries between I and II and between II and III are at  $\mathcal{T}_- \approx 0.551$  and  $\mathcal{T}_+ \approx 0.908$ , respectively. Regime II roughly corresponds to the negative-noise correction region.

probability distribution is shifted in the negative direction and the probability to find large current fluctuations is suppressed as compared with the noninteracting case [Fig. 10 (b)]. In the shaded area of Fig. 10 (a), the CGF is non-analytic and non-convex. Correspondingly, the rate function has a non-differentiable point at  $I = 0$ , see Fig. 10 (b). As a result, although the probability to observe currents smaller than the average value is enhanced by the inelastic phonon scattering, the probability to find negative currents  $I < 0$  is strongly suppressed. This is consistent with the FT (6), which states that although thermal agitations generate current flowing in the opposite direction to the source-drain bias, that current is exponentially suppressed at low temperatures.

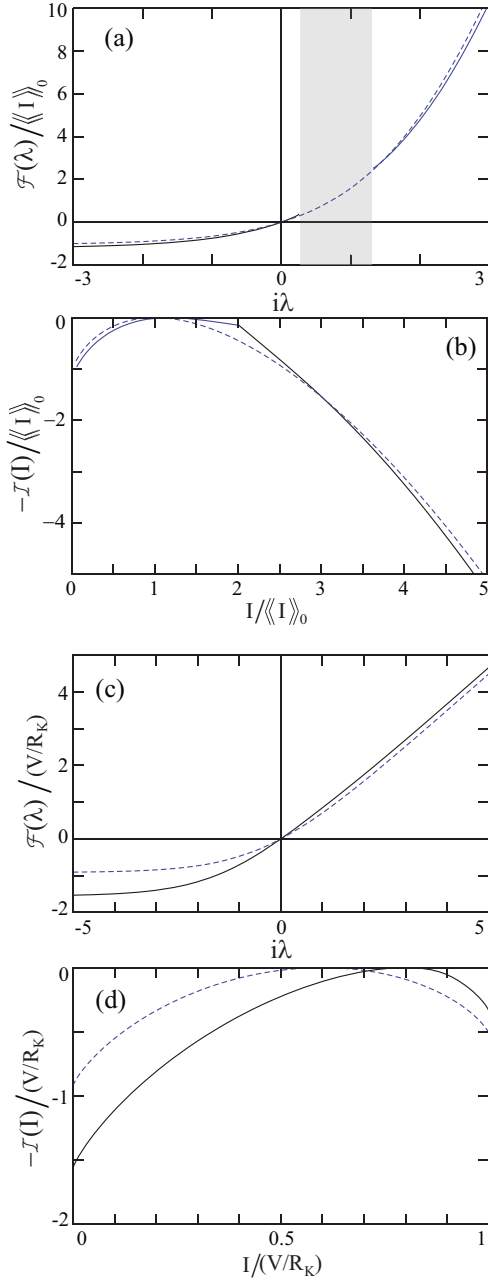


FIG. 9: The CGF (a) and the rate function (b) in I ( $\mathcal{T} = 0.1$ ). The solid lines are for  $g = 0.1$  and the dashed ones are for  $g = 0$ . The bias voltage is above threshold,  $V/\omega_0 = 1.5$ . Panels (c) and (d) show the CGF and the rate function, respectively, pertaining to II ( $\mathcal{T} = 0.6$ ). Axes notations are the same as in Fig. 7.

#### D. Discussion

Recently, Kumar *et al*<sup>5</sup> suggested to identify three regimes, based on the sign of the correction of the noise induced by the coupling to the phonons, as depicted in Fig. 8 (c). Our classification roughly agrees with that of Ref. 5, save for the transition points. The ones quoted

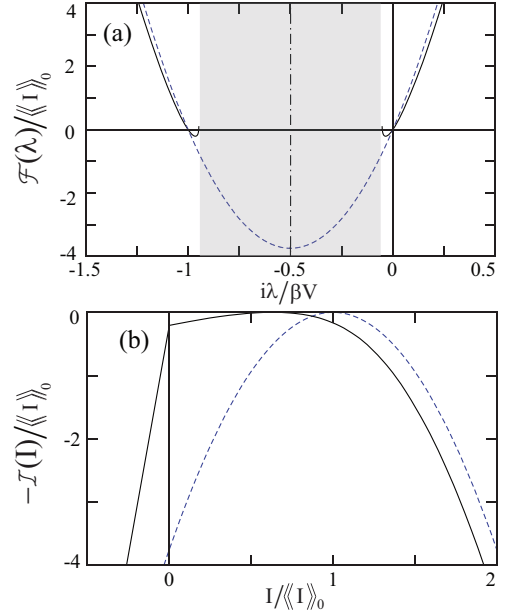


FIG. 10: (a) The CGF and (b) the rate function for  $\mathcal{T} = 1$ ,  $V/\omega_0 = 1.5$ , and  $\beta\omega_0 = 10$ . The dotted (solid) lines show results with ( $g = 0$ ) and without ( $g = 0.1$ ) electron-phonon interaction, respectively. In the shaded area of panel (a) the CGF for interacting case is non-analytic and non-convex, resulting in a non-differentiable point of the rate function at  $I = 0$  (b). Axes are normalized by  $\langle I \rangle_0 = V/R_K$ .

there,  $\mathcal{T}_{\pm}^{\text{Kumar}} = 1/2 \pm 1/(2\sqrt{2}) \approx 0.85, 0.15$ , are different from ours and moreover, our transition points  $\mathcal{T}_{\pm}$  depend on the bias voltage. Hence, there is no one-to-one correspondence between the classification of Ref. 5 and ours. Since oscillations in higher cumulants are ubiquitous<sup>20,53,55</sup> and dominated by locations of singularities, we think it would be legitimate to utilize the location distribution of singularities for the classification<sup>27–29</sup>.

A comment on the validity of second-order perturbation theory is called for. Flindt *et. al.*<sup>56</sup> analyzed the FCS of sequential transport through a quantum dot containing two levels.<sup>57</sup> They assume identical incoming rates but different outgoing rates for the two levels and analyzed the approximate CGF, obtained by expanding in the ratio of the two outgoing rates, taken to be a small parameter. They noticed a peculiar behavior: The agreement between the cumulants obtained by differentiating the approximate CGF (with respect to the counting field) and those derived by differentiating the CGF before expanding it was good for the low-order cumulants, but failed completely for the higher-order ones. In our case, the CGF is obtained as an expansion in the electron-phonon coupling and thus it is plausible that the unphysical results which we encountered around regime III for  $V > \omega_0$  at zero temperature, may have a similar origin to the apparent discrepancy reported in Ref. 56. This fault may be resolved by accounting for all orders in the electron-phonon coupling. However, getting analytical

results seems to be technically complicated and almost inevitably requires numerical methods.<sup>50</sup>

Another example of the FCS for interacting electron systems is found in transport through a quantum dot in the Kondo regime. Recently, Sakano *et al.* have calculated the CGF for the  $SU(N)$ -impurity Anderson model,<sup>18</sup> using the renormalized perturbation theory. Their result is exact up to the cubic order in the source-drain bias voltage  $\mathcal{O}(V^3)$  for a particle-hole symmetric case, and is quadratic in  $u$ . This is interpreted as the sum of the CGF for single-particle transfer and that for two-particle transfer. In our case, the phonon part of the CGF at zero temperature, to the leading order in  $V$ , can be obtained from Eqs. (62) and (69) in the form

$$\begin{aligned}\bar{\Phi}^{(2)} &\approx 2gV \sum_{n=1}^{\infty} \frac{\mathcal{T}^{n+1}}{(\mathcal{T}-1)^n} (u^n - 1) \\ &= \frac{2g\mathcal{T}(\mathcal{T}-1)(u-1)}{u-u_0} V, \end{aligned} \quad (76)$$

where  $u_0 = 1 - 1/\mathcal{T}$ . One may interpret the first right-hand side of Eq. (76) as a sum of independent  $n$ -electron transfers. However, the second line indicates that the CGF is non-analytic on the negative real axis of the  $u$ -plane at  $u_0 \leq 0$ . Therefore, the electron transfer statistics can be reduced to that of noninteracting electrons.<sup>26</sup> This example suggests subtleties in interpreting the CGF for interacting electrons.

## V. SUMMARY

We have investigated the full-counting statistics of currents mediated by elastic and inelastic electron-phonon scattering. In the extended wide-band limit, we obtained analytical expressions for the cumulant-generating function, accurate up to the second order in the electron-phonon coupling. Our analytic expressions are applicable for finite temperatures and bias voltages and satisfy the fluctuation theorem. Using those we analyzed the locations of singularities of the CGF. The singularities are symmetrically distributed in  $\lambda$ -plane because of the fluctuation theorem.

The singularities in  $u$ -plane, which appear because of the electron-phonon interaction, classify specific regimes in which the dependence of the electron transfer statistics, the current and the current noise, on the bare transmission is distinct. For small transmission probabilities we find singularities of the CGF on the positive real axis satisfying  $u > 1$ . Around the singularities, the CGF is non-convex, which results in a kink of the rate function. Such a kink, derived within the large-deviation analysis resembles a first-order phase transition in thermodynamics. It signifies the tendency of the phonon scattering to enhance the probability to find currents larger than the average value.

When the bias voltage is larger than the phonon frequency,  $V > \omega_0$ , we find singularities in  $0 < u < 1$

around perfect transmission. This results in a kink at  $I = 0$  of the rate function. Consequently the rate function is broadened because the probability to find currents smaller than the average value is enhanced. In the intermediate transmission probability region a negative correction in the current noise is induced by the inelastic electron-phonon scattering.

The kink structures in the rate function characterizes the electron-phonon interactions. Although measurements of the rate function would be technically demanding, the FCS can be in principle obtained experimentally,<sup>58</sup> giving hope that our predictions could be put to test.

## Acknowledgments

We thank Christian Flindt, Dimitri Golubev and Akira Oguri for valuable discussions. This work was supported by the Binational Science Foundation and by the Israel Academy of Science, the Okasan-Katoh Foundation, Grant-in-Aid for Young Scientists (B) (No. 23740294 and No. 24710111), Young Researcher Overseas Visits Program for Vitalizing Brain Circulation (R2214) from the JSPS and MEXT kakenhi "Quantum Cybernetics".

## Appendix A: The Luttinger-Ward potential

The way to construct a partition function based on the self energy is to exploit the Luttinger-Ward functional approach,<sup>46</sup> or the self-consistent  $\Phi$ -derivable approximation.<sup>45</sup> This method can be straightforwardly extended to a nonequilibrium situation.<sup>47</sup> The saddle-point approximation for the CGF can also be constructed by this approach.<sup>44</sup> The underlying idea is the observation that by introducing the Luttinger-Ward functional  $\Phi$ , which includes all skeleton diagrams, the total generating functional can be formally written as

$$\mathcal{F}(\lambda) = \lim_{\tau \rightarrow \infty} \frac{1}{\tau} \left( \text{Tr}[\ln G^{-1}] + \text{Tr}[\Sigma(G)G] - \Phi(G) \right), \quad (\text{A1})$$

where the trace and the product mean integrations over time along the Keldysh contour. The Green function  $G$ , also defined on the Keldysh contour, is

$$G^{-1}(1, 2) = g_{\lambda}^{-1}(1, 2) - \Sigma(1, 2; G), \quad (\text{A2})$$

where the arguments  $1, 2, \dots$  stand for  $t_1, t_2, \dots$ . Here  $g_{\lambda}$  is the Green function of the noninteracting electrons

$$g_{\lambda}(1, 2) = -i \langle T_K c_0(1) c_0^{\dagger}(2) \rangle, \quad (\text{A3})$$

given explicitly in Eqs. (22) and (23). The self energy is a functional of  $G$  as well as of the phonon Green function  $d$ ,

$$d(1, 2) = -i \langle T_K (b(1)_I + b^{\dagger}(1)_{\bar{I}})(b(2)_I + b^{\dagger}(2)_{\bar{I}}) \rangle, \quad (\text{A4})$$

given in Eqs. (40) and (41). The functional derivative of the nonequilibrium Luttinger-Ward functional  $\Phi$  gives the self energy,

$$\Sigma(1, 2; G) = \frac{\delta\Phi}{\delta G(2, 1)}. \quad (\text{A5})$$

Both functions  $G$  and  $\Sigma$  depend implicitly on the counting field only through  $g_\lambda$ .

By differentiating Eq. (A1) with respect to the counting field  $\lambda$  and using Eq. (A5) one obtains

$$\frac{d\mathcal{F}(\lambda)}{d\lambda} = - \lim_{\tau \rightarrow \infty} \frac{1}{\tau} \text{Tr} \left( G \frac{\partial g_\lambda^{-1}}{\partial \lambda} \right), \quad (\text{A6})$$

where we have used the relation

$$\frac{d\Phi}{d\lambda} = \text{Tr} \left( \frac{\delta\Phi}{\delta G} \frac{\partial G}{\partial \lambda} \right). \quad (\text{A7})$$

It should be emphasized that in this formulation the self energy has to be determined self-consistently in order to satisfy conservation laws.<sup>47</sup> To second order in the electron-phonon coupling  $\gamma$ , Eq. (A6) becomes

$$\begin{aligned} \frac{d\mathcal{F}}{d\lambda} &\approx \lim_{\tau \rightarrow \infty} \frac{1}{\tau} \text{Tr} \left( g_\lambda \frac{\partial g_\lambda^{-1}}{\partial \lambda} \right) \\ &+ \lim_{\tau \rightarrow \infty} \frac{1}{\tau} \text{Tr} \left( g_\lambda \Sigma(g_\lambda) g_\lambda \frac{\partial g_\lambda^{-1}}{\partial \lambda} \right), \end{aligned} \quad (\text{A8})$$

where we have replaced  $\Sigma(G)$  by  $\Sigma(g_\lambda)$ , since it is already  $\mathcal{O}(\gamma^2)$ . Upon using the identity

$$\frac{\partial g_\lambda}{\partial \lambda} = -g_\lambda \frac{\partial g_\lambda^{-1}}{\partial \lambda} g_\lambda, \quad (\text{A9})$$

and exploiting Eq. (A5) [in its  $\mathcal{O}(\gamma^2)$  form] Eq. (A8) becomes

$$\frac{d\mathcal{F}}{d\lambda} \approx \lim_{\tau \rightarrow \infty} \frac{1}{\tau} \frac{d}{d\lambda} \text{Tr}[\ln g_\lambda^{-1}] - \lim_{\tau \rightarrow \infty} \frac{1}{\tau} \frac{d\Phi(g_\lambda)}{d\lambda}, \quad (\text{A10})$$

and consequently

$$\mathcal{F}(\lambda) = \lim_{\tau \rightarrow \infty} \frac{1}{\tau} \left( \text{Tr}[\ln g_\lambda^{-1}] \right) - \bar{\Phi}^{(2)}(\lambda). \quad (\text{A11})$$

Comparing this expression with the original one, Eq. (A1), one notes that the term depending explicitly on the self energy has disappeared. The lowest-order scaled Luttinger-Ward potential  $\bar{\Phi}^{(2)}(\lambda)$  is obtained by expanding  $\bar{\Phi}(g_\lambda)$  (which depends on  $g_\lambda$  and not on  $G$ ) up to  $\mathcal{O}(\gamma^2)$  [see Eq. (18)].

For brevity, the calculation above is presented in the time domain. One may also switch to the frequency representation in which Eq. (A6) reads

$$\frac{d\mathcal{F}(\lambda)}{d\lambda} = -\frac{1}{2\pi} \int d\omega \text{Tr} \left( G(\omega) \tau_3 \frac{\partial g_\lambda(\omega)^{-1}}{\partial \lambda} \tau_3 \right).$$

The Pauli matrix  $\tau_3$ , Eq. (47), appears once we project the time from the Keldysh contour on the real time axis,

$$\int_K dt = \int_{-\tau/2}^{\tau/2} dt_+ - \int_{-\tau/2}^{\tau/2} dt_-, \quad (\text{A12})$$

where  $t_\pm \in K_\pm$  (see Fig. 3). This leads to Eqs. (16) and (17) in the main text.

It remains to calculate  $\bar{\Phi}(g_\lambda)$  up to  $\mathcal{O}(\gamma^2)$ . This is accomplished by expanding it perturbatively in  $\gamma$ . The zeroth-order term is just a constant,

$$\bar{\Phi}^{(0)}(g_\lambda) = - \lim_{\tau \rightarrow \infty} \frac{1}{2\tau} \text{Tr} \ln[d], \quad (\text{A13})$$

independent of the counting field. The diagrams constituting the second order are depicted in Fig. 4. The Hartree term [Fig. 4 (a)] is

$$\begin{aligned} \bar{\Phi}^H(g_\lambda) &= -i \frac{\gamma^2}{2} \lim_{\tau \rightarrow \infty} \frac{1}{\tau} \int_K d1 d2 g_\lambda(1, 1) d(1, 2) g_\lambda(2, 2) \\ &= -i \frac{\gamma^2}{2} \sum_{s, s' = +, -} s s' d^{ss'}(0) \int d\omega_1 g_\lambda^{ss}(\omega_1) \int d\omega_2 g_\lambda^{s's'}(\omega_2). \end{aligned} \quad (\text{A14})$$

Inserting Eqs. (23) and (41) into Eq. (A14) yields

$$\begin{aligned} \bar{\Phi}^H(g_\lambda) &= \frac{4\pi g}{\omega_0} \left( \int d\omega \frac{1}{\Omega_\lambda(\omega)} \frac{\Gamma(\omega - \epsilon_0)}{(\omega - \epsilon_0)^2 + \Gamma^2/4} \right) \\ &\times \left( \sum_r \frac{\Gamma_r}{\Gamma} \int d\omega \bar{\rho}(\omega) \frac{2f_r^+(\omega) - 1}{\Omega_\lambda(\omega)} \right), \end{aligned} \quad (\text{A15})$$

where the small parameter  $g$  is given in Eq. (43). Note the appearance of the distribution Eq. (21) in the form  $f_r^+(\omega) - 1/2$ , resulting from the definition of the step function as  $\Theta(0) = 1/2$  in the continuous notation.<sup>59</sup> By using Eq. (37), one can check that the FT is fulfilled,  $\bar{\Phi}^H(g_{-\lambda+i\beta V}) = \bar{\Phi}^H(g_\lambda)$ . In the main text, we neglect the Hartree term since it does not depend on the phonon distribution.

The Fock term [Fig. 4 (b)] reads

$$\begin{aligned} \bar{\Phi}^F(g_\lambda) &= i \frac{\gamma^2}{2} \lim_{\tau \rightarrow \infty} \frac{1}{\tau} \int_K d1 d2 g_\lambda(1, 2) d(1, 2) g_\lambda(2, 1) \\ &= -\frac{1}{2} \lim_{\tau \rightarrow \infty} \frac{1}{\tau} \int_K d1 d2 d(1, 2) \Pi_\lambda(2, 1), \end{aligned} \quad (\text{A16})$$

where we have introduced the particle-hole propagator,  $\Pi$ ,

$$\Pi_\lambda(1, 2) = -i \gamma^2 g_\lambda(1, 2) g_\lambda(2, 1). \quad (\text{A17})$$

Adopting the form (A16), we find



$$\bar{\Phi}^F(g_\lambda) = -\frac{1}{2} \int \frac{d\omega}{2\pi} \left[ d^{++}(\omega) \Pi_\lambda^{++}(\omega) + d^{--}(\omega) \Pi_\lambda^{--}(\omega) - d^{-+}(\omega) \Pi_\lambda^{+-}(\omega) - d^{+-}(\omega) \Pi_\lambda^{-+}(\omega) \right]. \quad (\text{A18})$$

Here a constant should be added to keep the normalization condition  $\bar{\Phi}^F(g_0) = 0$ . Inserting Eqs. (53) and (54), we obtain

$$\begin{aligned} \bar{\Phi}^F(g_\lambda) = & -\frac{1}{2} \int \frac{d\omega}{2\pi} \left[ d^{-+}(\omega) \left( \frac{\tilde{\Pi}_\lambda^{+-}(\omega) + \Pi_0^{+-}(\omega)}{2} - \Pi_\lambda^{+-}(\omega) \right) + d^{+-}(\omega) \left( \frac{\tilde{\Pi}_\lambda^{-+}(\omega) + \Pi_0^{-+}(\omega)}{2} - \Pi_\lambda^{-+}(\omega) \right) \right. \\ & \left. + \frac{d^{-+}(\omega) + d^{+-}(\omega)}{2} \phi_\lambda^S(\omega) + \frac{d^{++}(\omega) - d^{--}(\omega)}{2} \phi_\lambda^A(\omega) \right]. \end{aligned} \quad (\text{A19})$$

Using relations (50) and the corresponding ones for the components of the phonon Green function, e.g.,  $d^{+-}(\omega) = d^{-+}(-\omega)$ , yields

$$\bar{\Phi}^F(g_\lambda) = \sum_{s=\pm} s n^+(s\omega_0) \left( \frac{i\tilde{\Pi}_\lambda^{+-}(s\omega_0) + i\Pi_0^{+-}(s\omega_0)}{2} - i\Pi_\lambda^{+-}(s\omega_0) \right) + \frac{i}{2} \coth\left(\frac{\beta\omega_0}{2}\right) \phi_\lambda^S(\omega_0) - \text{P} \int \frac{d\omega}{2\pi} \frac{\omega_0 \phi_\lambda^A(\omega)}{\omega^2 - \omega_0^2}, \quad (\text{A20})$$

where P means Cauchy principle value. By using Eqs. (65) and (B13), one may verify that the FT is obeyed,  $\bar{\Phi}^F(g_{-\lambda+i\beta V}) = \bar{\Phi}^F(g_\lambda)$ .

The Fock term depends on the equilibrium phonon distribution  $n^+$ ,<sup>19,21</sup> which suggests that a resummation of an infinite series of diagrams is needed in order to account for the nonequilibrium phonon distribution. We carry out this summation within the random-phase approximation, by summing over all ring diagrams [see diagrams (c) and (d) in Fig. 4]. The RPA is also known to be relevant for the AC conductance.<sup>60</sup> In this way, we obtain the functional

$$\begin{aligned} \bar{\Phi}^{\text{RPA}}(g_\lambda) &= \frac{1}{2} \lim_{\tau \rightarrow \infty} \frac{1}{\tau} \text{Tr} \ln [1 - d \Pi_\lambda] + \bar{\Phi}^{(0)}(g_\lambda) \\ &= \frac{1}{2} \lim_{\tau \rightarrow \infty} \frac{1}{\tau} \text{Tr} \ln D_\lambda^{-1}, \end{aligned} \quad (\text{A21})$$

where we have also included the zeroth-order term, Eq. (A13) and the full phonon propagator,  $D_\lambda$ ,

$$D_\lambda^{-1} = d^{-1} - \Pi_\lambda. \quad (\text{A22})$$

Equation (A21) yields Eq. (44) in Fourier space.

This RPA can be also formulated using the Keldysh path-integral approach within the saddle-point approximation<sup>44</sup> and further accounting for the Gaussian-fluctuation correction around it.

## Appendix B: Analytic expressions for the particle-hole propagator

Here we obtain analytic expressions for the four components of the particle-hole propagator, Eqs. (49), in the extended wide-band limit.<sup>19</sup> Since the lesser and greater components are related to one another [see Eqs. (50)] it suffices to compute the greater function, which reads

$$i\tilde{\Pi}_{rr'}^{+-}(\omega) \approx g\alpha_{rr'}\rho_0^2 \int d\omega' \frac{f_r^-(\omega_+) f_{r'}^+(\omega_-)}{\Omega_\lambda(\omega_+) \Omega_\lambda(\omega_-)}, \quad (\text{B1})$$

where the small parameter  $g$  is given in Eq. (43), and

$$\omega_\pm = \omega' \pm \omega/2, \quad (\text{B2})$$

A lengthy calculation yields

$$i\tilde{\Pi}_{rr'}^{+-}(\omega) = \frac{g\alpha_{rr'}\rho_0^2}{\beta} e^{\beta(\omega+s_r V)/2} \sum_i (z_i + e^{-\beta(s_r V + \omega)/2}) (z_i + e^{-\beta(s_r' V - \omega)/2}) \log z_i \prod_{j \neq i} \frac{1}{z_i - z_j}, \quad (\text{B3})$$

where  $s_r = \pm 1$  for  $r = L/R$ ,

$$z_1 = e^{\beta\omega/2} Z_{\lambda+}, \quad z_2 = e^{\beta\omega/2} Z_{\lambda-}, \quad z_3 = e^{-\beta\omega/2} Z_{\lambda+}, \quad z_4 = e^{-\beta\omega/2} Z_{\lambda-},$$

and  $Z_{\lambda\pm}$  are given by Eqs. (33). The calculation of  $\Pi^{++}$  and  $\Pi^{--}$  is facilitated by considering the combina-

tions  $\Pi^{++} \pm \Pi^{--}$ . The only  $\lambda$ -dependence of the casual

and anti-casual electronic Green functions is contained in their denominator,  $\Omega_\lambda$  [see Eqs. (23)]. Therefore we may write

$$i\Pi_\lambda^{\pm\pm}(\omega) = \frac{\gamma^2}{2\pi} \int d\omega' \frac{g_0^{\pm\pm}(\omega_+)g_0^{\pm\pm}(\omega_-)}{\Omega_\lambda(\omega_+)\Omega_\lambda(\omega_-)}. \quad (\text{B4})$$

Upon using the relations

$$\begin{aligned} g_0^{++} &= g_0^{+-} + g^R = g_0^{-+} + g^A, \\ g_0^{--} &= g_0^{-+} - g^R = g_0^{+-} - g^A, \end{aligned} \quad (\text{B5})$$

where  $g^{R,A}$  are the retarded and advanced Green functions,

$$g^{R,A}(\omega) = \frac{1}{\omega - \epsilon_0 \pm i\Gamma/2}, \quad (\text{B6})$$

we find Eq. (53) with

$$\begin{aligned} i\phi_\lambda^S(\omega) &= \frac{\gamma^2}{2\pi} \int d\omega' \left( \frac{1}{\Omega_\lambda(\omega_+)\Omega_\lambda(\omega_-)} - 1 \right) \\ &\times [g^R(\omega_+)g^R(\omega_-) + g^A(\omega_+)g^A(\omega_-)], \end{aligned} \quad (\text{B7})$$

where the relation

$$\int d\omega' g^{R/A}(\omega_+)g^{R/A}(\omega_-) = 0 \quad (\text{B8})$$

has been used. Since  $\Omega_\lambda = 1$  for  $|\omega| \gg \max(|V|, 1/\beta)$  the integral in Eq. (B7) is bounded, and therefore in the extended wide-band limit<sup>19</sup> the terms in the square brackets there can be replaced by

$$2\text{Re } g^R(0)^2 \approx \begin{cases} 8\rho_0[1 - 2\rho_0]/\Gamma^2 & (|V|, k_B T, \omega_0 \ll \Gamma) \\ 2/\epsilon_0^2 & (|V|, k_B T, \omega_0, \Gamma \ll |\epsilon_0|) \end{cases}, \quad (\text{B9})$$

yielding

$$i\phi_\lambda^S(\omega) \approx \begin{cases} 2g\rho_0[1 - 2\rho_0]S & (|V|, k_B T, \omega_0 \ll \Gamma) \\ 0 & (|V|, k_B T, \omega_0, \Gamma \ll |\epsilon_0|) \end{cases}, \quad (\text{B10})$$

where

$$\begin{aligned} S &= \int d\omega' \left( \frac{1}{\Omega_\lambda(\omega_+)\Omega_\lambda(\omega_-)} - 1 \right) \\ &= \sum_i \left( \prod_{s,s'=\pm} (e^{\beta(sV+s'\omega)/2} + z_i) \right) \frac{\log z_i}{\beta z_i} \prod_{j \neq i} \frac{1}{z_j - z_i}. \end{aligned} \quad (\text{B11})$$

Turning now to the combination  $\Pi^{++} - \Pi^{--}$ , we use Eqs. (B5) and the relation  $g^K = g_0^{-+} + g_0^{+-}$  for the Keldysh component of the Green function, to obtain Eq. (54). Equation (55) is derived from the relation

$$\Pi^R(\omega) = \frac{\gamma^2}{2\pi i} \int d\omega' \frac{g^K(\omega_+)g^A(\omega_-) + g^R(\omega_+)g^K(\omega_-)}{2}.$$

In Eq. (54), we obtain,

$$\begin{aligned} i\phi_\lambda^A(\omega) &= \frac{\gamma^2}{2\pi} \int d\omega' \left( \frac{1}{\Omega_\lambda(\omega_+)\Omega_\lambda(\omega_-)} - 1 \right) \\ &\times \text{Im} \left( g^K(\omega_+)g^A(\omega_-) + g^R(\omega_+)g^K(\omega_-) \right). \end{aligned} \quad (\text{B12})$$

Using Eq. (37), we can verify the symmetry

$$\phi_{-\lambda+i\beta V}^A(\omega) = \phi_\lambda^A(\omega). \quad (\text{B13})$$

One can now convince oneself that in the extended wide-band limit, in which  $\text{Re}[g^R(\omega)] \approx -\epsilon_0/[\epsilon_0^2 + \Gamma^2/4]$  and

$$g^K(\omega) = -\frac{4i}{\Gamma} \sum_r \frac{\Gamma_r}{\Gamma} \rho_0 \tanh[\beta(\omega - \mu_r)/2] \quad (\text{B14})$$

is  $\mathcal{O}(1/\Gamma)$ ,  $\phi_\lambda^A$  may be safely neglected, since

$$\phi_\lambda^A \propto \begin{cases} 1/\Gamma^2 & (|V|, k_B T, \omega_0 \ll \Gamma) \\ 1/(\Gamma|\epsilon_0|) & (|V|, k_B T, \omega_0, \Gamma \ll |\epsilon_0|) \end{cases}. \quad (\text{B15})$$

\* Electronic address: utsumi@phen.mie-u.ac.jp

† Also at Tel Aviv University.

<sup>1</sup> R. H. M. Smit, Y. Noat, C. Untiedt, N. D. Lang, M. C. van Hemert, and J. M. van Ruitenbeek, *Nature* **419**, 906 (2002).

<sup>2</sup> M. Kiguchi, O. Tal, S. Wohlthat, F. Pauly, M. Krieger, D. Djukic, J. C. Cuevas, and J. M. van Ruitenbeek, *Phys. Rev. Lett.* **101**, 046801 (2008).

<sup>3</sup> O. Tal, M. Krieger, B. Leerink, J. M. van Ruitenbeek, *Phys. Rev. Lett.* **100**, 196804 (2008).

<sup>4</sup> N. Agrait, C. Untiedt, G. Rubio-Bollinger, and S. Vieira, *Phys. Rev. Lett.* **88**, 216803 (2002).

<sup>5</sup> M. Kumar, R. Avriller, A. Levy Yeyati, and J. M. van

Ruitenbeek, *Phys. Rev. Lett.* **108**, 146602 (2012).

<sup>6</sup> J. K. Viljas, J. C. Cuevas, F. Pauly, and M. Häfner, *Phys. Rev. B* **72**, 245415 (2005).

<sup>7</sup> T. Frederiksen, M. Brandbyge, N. Lorente, and A.-P. Jauho, *Phys. Rev. Lett.* **93**, 256601 (2004).

<sup>8</sup> M. Galperin, M. A. Ratner, and A. Nitzan, *J. Phys. Cond. Matt.* **19**, 103201 (2007).

<sup>9</sup> R. Egger and A. O. Gogolin, *Phys. Rev. B* **77**, 113405 (2008); O. Entin-Wohlman, Y. Imry, and A. Aharony, *Phys. Rev. B* **80**, 035417 (2009).

<sup>10</sup> T. Holstein, *Ann. Phys.* **8**, 325 (1959).

<sup>11</sup> R. Avriller and A. Levy Yeyati, *Phys. Rev. B* **80**, 041309(R) (2009).

- <sup>12</sup> L. S. Levitov and G. B. Lesovik, JETP Lett. **58**, 230 (1993); L. S. Levitov, H. Lee, and G. B. Lesovik, J. Math. Phys. **37**, 4845 (1996).
- <sup>13</sup> *Quantum Noise in Mesoscopic Physics, Vol. 97 of NATO Science Series II: Mathematics, Physics and Chemistry* edited by Yu. V. Nazarov (Kluwer Academic Publishers, Dordrecht/Boston/London, 2003).
- <sup>14</sup> A. Komnik and A. O. Gogolin, Phys. Rev. Lett. **94**, 216601 (2005); A. O. Gogolin and A. Komnik, Phys. Rev. B **73**, 195301 (2006).
- <sup>15</sup> D. A. Bagrets, Y. Utsumi, D. S. Golubev, and G. Schön, Fortschr. Phys. **4**, 917 (2006).
- <sup>16</sup> D. A. Bagrets, Phys. Rev. Lett. **93**, 236803 (2004).
- <sup>17</sup> Y. Utsumi, D. S. Golubev, and G. Schön, Phys. Rev. Lett. **96**, 086803 (2006).
- <sup>18</sup> R. Sakano, Y. Nishikawa, A. Oguri, A. C. Hewson, S. Tarucha, Phys. Rev. Lett. **108**, 266401 (2012); R. Sakano, A. Oguri, T. Kato, and S. Tarucha, Phys. Rev. B **83**, 241301 (2011).
- <sup>19</sup> F. Haupt, T. Novotný, and W. Belzig, Phys. Rev. Lett. **103**, 136601 (2009); F. Haupt, T. Novotný, and W. Belzig, Phys. Rev. B **82**, 165441 (2010); T. Novotný, F. Haupt, and W. Belzig, Phys. Rev. B **84**, 113107 (2011).
- <sup>20</sup> T. L. Schmidt and A. K. Komnik, Phys. Rev. B **80**, 041307(R) (2009).
- <sup>21</sup> D. F. Urban, R. Avriller, and A. Levy Yeyati, Phys. Rev. B **82**, 121414(R) (2010).
- <sup>22</sup> L. Simine and D. Segal, arxiv:1203.3910.
- <sup>23</sup> G. Schaller, T. Krause, T. Brandes, M. Esposito, arXiv:1206.3960.
- <sup>24</sup> S. Maier, T. L. Schmidt, and A. Komnik, Phys. Rev. B **83**, 085401 (2011).
- <sup>25</sup> H. Touchette, Phys. Rep. **478**, 1 (2009).
- <sup>26</sup> A. G. Abanov and D. A. Ivanov, Phys. Rev. Lett. **100**, 086602 (2008); A. G. Abanov and D. A. Ivanov, Phys. Rev. B **79**, 205315 (2009).
- <sup>27</sup> D. Kambly, C. Flindt, and M. Büttiker, Phys. Rev. B **83**, 075432 (2011).
- <sup>28</sup> D. A. Ivanov, A. G. Abanov, Europhys. Lett. **92**, 37008 (2010).
- <sup>29</sup> C. Flindt and J. P. Garrahan, arXiv:1209.2524.
- <sup>30</sup> C. N. Yang and T. D. Lee, Phys. Rev. **87**, 404 (1952); T. D. Lee and C. N. Yang, Phys. Rev. **87**, 410 (1952).
- <sup>31</sup> M. Vanević, Yu. V. Nazarov, and W. Belzig, Phys. Rev. Lett. **99**, 076601 (2007).
- <sup>32</sup> F. Hassler, M. V. Suslov, G. M. Graf, M. V. Lebedev, G. B. Lesovik, and G. Blatter, Phys. Rev. B **78**, 165330 (2008).
- <sup>33</sup> D. J. Evans, E. G. D. Cohen, and G. P. Morriss, Phys. Rev. Lett. **71**, 2401 (1993); *ibid.* **71**, 3616 (1993); G. Gallavotti and E. G. D. Cohen, Phys. Rev. Lett. **74**, 2694 (1995); G. Gallavotti, Phys. Rev. Lett. **77**, 4334 (1996).
- <sup>34</sup> J. Tobiska and Yu. V. Nazarov, Phys. Rev. B **72**, 235328 (2005).
- <sup>35</sup> H. Förster and M. Büttiker, Phys. Rev. Lett. **101**, 136805 (2008).
- <sup>36</sup> K. Saito and Y. Utsumi, Phys. Rev. B **78**, 115429 (2008); arXiv:0709.4128.
- <sup>37</sup> D. Andrieux, P. Gaspard, T. Monnai, and S. Tasaki, New J. Phys. **11** 043014 (2009).
- <sup>38</sup> M. Esposito, U. Harbola, and S. Mukamel, Rev. Mod. Phys. **81**, 1665 (2009).
- <sup>39</sup> M. Campisi, P. Hänggi, and M. Talkner, Rev. Mod. Phys. **83**, 771 (2011).
- <sup>40</sup> A. Altland, A. De Martino, R. Egger, and B. Narozhny, Phys. Rev. Lett. **105**, 170601 (2010); Phys. Rev. B **82**, 115323 (2010).
- <sup>41</sup> Y. Utsumi, D. S. Golubev, M. Marthaler, K. Saito, T. Fujisawa, and G. Schön, Phys. Rev. B **81**, 125331 (2010); B. Küng, C. Rössler, M. Beck, M. Marthaler, D. S. Golubev, Y. Utsumi, T. Ihn, and K. Ensslin, Phys. Rev. X **2**, 011001 (2012).
- <sup>42</sup> S. Nakamura, Y. Yamauchi, M. Hashisaka, K. Chida, K. Kobayashi, T. Ono, R. Leturcq, K. Ensslin, K. Saito, Y. Utsumi, and A. C. Gossard, Phys. Rev. Lett. **104**, 080602 (2010); Phys. Rev. B **83**, 155431 (2011).
- <sup>43</sup> O.-P. Saira, Y. Yoon, T. Tanttu, M. Möttönen, D. V. Averin, J. P. Pekola, arXiv:1206.7049.
- <sup>44</sup> Y. Utsumi and K. Saito, Phys. Rev. B **79**, 235311 (2009).
- <sup>45</sup> G. Baym and L. P. Kadanoff, Phys. Rev. **124**, 287 (1961); G. Baym, Phys. Rev. **127**, 1391 (1962).
- <sup>46</sup> J. M. Luttinger and J. C. Ward, Phys. Rev. **118**, 5 (1960); J. M. Luttinger, Phys. Rev. **119**, 4 (1960).
- <sup>47</sup> Yu. B. Ivanov, J. Knoll, H. Van Hees, and D. N. Voskresensky, Nucl. Phys. A **657**, 413 (1999).
- <sup>48</sup> C. M. Bender and S. A. Orszag, *Advanced Mathematical Methods for Scientists and Engineers*, (Springer, New York, 1999).
- <sup>49</sup> A. Mitra, I. Aleiner, and A. J. Millis, Phys. Rev. B **69**, 245302 (2004).
- <sup>50</sup> T.-H. Park and M. Galperin, Phys. Rev. B **84**, 205450 (2011).
- <sup>51</sup> O. Entin-Wohlman, Y. Imry, and A. Aharony, Phys. Rev. B **81**, 113408 (2010).
- <sup>52</sup> A. Rosch, J. Paaske, J. Kroha, and P. Wölffe, Phys. Rev. Lett. **90**, 076804 (2003); O. Parcollet and C. Hooley, Phys. Rev. B **66**, 085315 (2002).
- <sup>53</sup> C. Flindt, C. Fricke, F. Hohls, T. Novotný, K. Netočný, T. Brandes, and R. J. Haug, Proc. Natl. Acad. Sci. USA **106**, 10116 (2009).
- <sup>54</sup> J. L. Lebowitz and H. Spohn, J. Stat. Phys. **95**, 333 (1999).
- <sup>55</sup> D. S. Golubev, M. Marthaler, Y. Utsumi, Gerd Schön, Phys. Rev. B **81**, 184516 (2010).
- <sup>56</sup> C. Flindt, T. Novotný, A. Braggio, and A.-P. Jauho, Phys. Rev. B **82**, 155407 (2010).
- <sup>57</sup> W. Belzig, Phys. Rev. B **71**, 161301(R) (2005).
- <sup>58</sup> Y. Utsumi, D. S. Golubev, M. Marthaler, G. Schön, K. Kobayashi, Phys. Rev. B **86**, 075420 (2012).
- <sup>59</sup> For a precise treatment of the step function, see Sec. 2.8 in A. Kamenev, *Field Theory of Nonequilibrium Systems* (Cambridge University Press, Cambridge, 2011).
- <sup>60</sup> A. Ueda, O. Entin-Wohlman, and A. Aharony, Phys. Rev. B **83**, 155438 (2011).